Thus it is not unreasonable to believe that the haloed C_1 crater is a true, recent hypervelocity feature of meteoritic origin, while the larger C_2 crater is the man-made feature produced by the Ranger VIII spacecraft. This conclusion is buttressed by the fact that the larger crater appears to be surrounded by material, some of it rayed, having a lower albedo than that typical of the general region. The anomalous dark material turned up by the impact of the Surveyor I footpads immediately comes to mind. The Ranger VIII impact was not at hypervelocity.

It thus appears highly probable that the C_2 crater is the one produced by Ranger VIII. This crater is 13 m in diameter, in such close agreement with the fourth-root gravity scaling that the latter is probably correct. If fourth-root gravity scaling is correct, it implies that the outer layers of the moon's surface are composed of materials whose cohesiveness is close to that of terrestrial soils, much as Surveyor III has shown them to be. The results of Moraski *et al.* (*8*) would appear not to apply to the Ranger VIII crater.

It should also be pointed out that gravity scaling as here exemplified is effective only when the materials can be put into ballistic trajectories. When compression is the major cratering effect, we are dealing with strength of materials and with mass, which are not functions of gravity. Hence gravity scaling should be a major factor only for those craters formed largely within the outer soil-like layers of the moon. The much larger craters will approach more closely to the size craters the same meteorites would produce on the earth for the same velocity of impact.

RALPH B. BALDWIN

Oliver Machinery Company,
Grand Rapids, Michigan

References and Notes

1. B. P. Huber, personal communication, 31 January 1967.
2. Ranger VIII photographs of the moon, NASA SP-111. Prepared under contract for NASA by Jet Propulsion Laboratory, California Institute of Technology, 1966.
3. R. B. Baldwin, *The Measure of the Moon* (Univ. of Chicago Press, Chicago, 1963), p. 162.
4. ———, *ibid.*, p. 141.
5. J. D. Halajian, J. Reichman, L. L. Karafiath, *Grumman Research Dept. Report RE-280, Correlation of Mechanical and Thermal Properties of Extraterrestrial Materials,* January 1967.
6. D. E. Gault and H. J. Moore, paper presented at the 7th Hypervelocity Impact Symposium, Tampa, Florida, November 1964.
7. A. J. Chabai, *J. Geophys. Res.* **70**, 20, 5075 (1965).
8. L. K. Moraski, D. J. Teal, J. E. Lynch, C. J. Higgins, S. W. Johnson, abstract in *Trans. Amer. Geophys. Union,* **47**, 1, 149 (1966).
9. D. E. Gault, personal communication, 7 April 1967.

14 June 1967

Distortion of a Splashing Liquid Drop

Abstract. *The low-speed splash of a drop of liquid into a pool can result in a surprisingly complicated flow pattern, apparently not detected by previous experiments or theories. We examined the dynamics of this process by high-speed computer, obtaining a series of configuration plots at various stages of the splash.*

The dynamics of a liquid drop splashing into a pool have been studied experimentally (*1–4*) and by numerical solution of the Navier-Stokes equations (*5*). The experimental results have been obtained principally by high-speed photography. They show especially well the behavior of the free surface through the following sequence of events: (i) A crater is formed and fluid

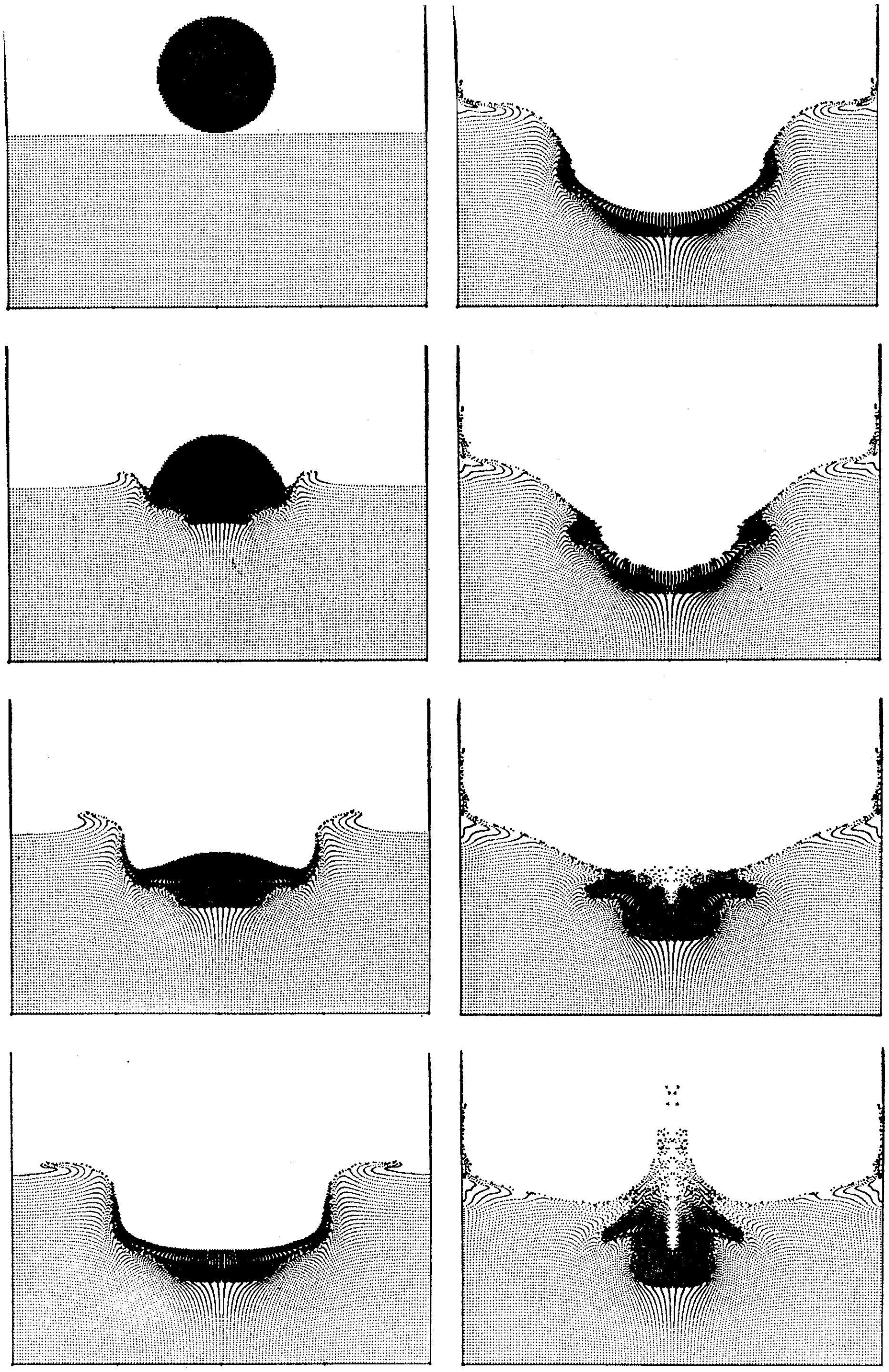

Fig. 1. Cross section of splashing drop with u_0 = 2.0. Frames (read left, down; right, down) are at t = 0, 5, 10, 15, 20, 25, 30, and 35.

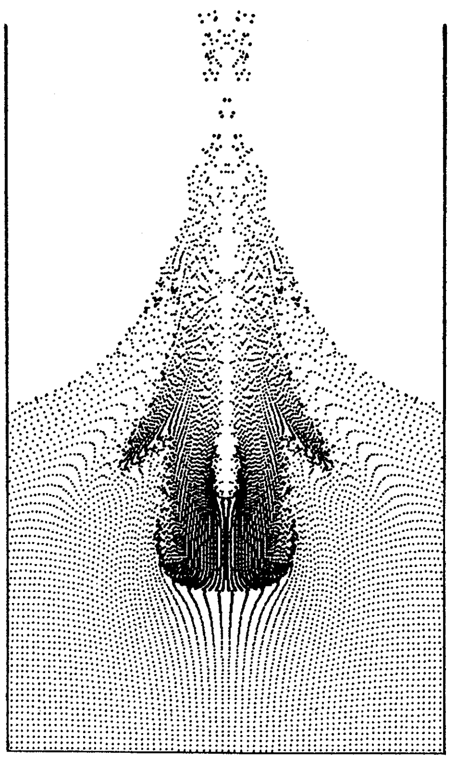

Fig. 2. Enlargement of the calculation shown in Fig. 1, for $t = 45$.

splashes to the side. (ii) Fluid rushes back to fill the crater. (iii) A jet column is formed along the collapse axis. (iv) The jet column rises well above the initial pool surface and may break into several droplets. (v) The jet column falls back, creating a second crater and lateral wave.

The fluid originally in the drop may ultimately separate into two parts or remain together, depending on the impact speed (*2*). Some of it is carried up into the jet column, but much is left imbedded in the pool (*5*). We present here the striking configuration that can be attained by the imbedded drop material if the impact velocity is within a certain range.

For a pool of essentially infinite depth, and in the absence of viscosity and surface tension, the crucial parameter for drop impact scaling can be written in the form $(gR)^{1/2}/u_0$, in which g is the gravitational acceleration, R is the drop radius, and u_0 is the impact speed. [For a drop that has fallen freely from a height h, prior to impact, then this parameter is also equal to $(R/2h)^{1/2}$.]

To examine the splash dynamics in detail, we used the Marker-and-Cell computing technique described in several publications (*6, 7*); hence, only a brief description is given here. The full Navier-Stokes equations are written in finite difference form, retaining the velocity components and pressure as the dependent variables. The calculation advances in time from prescribed initial conditions through a set of finite time intervals, or cycles. Each cycle consists of (i) solving a Poisson's equation for the pressures, (ii) using these to solve for the changes in velocity, and (iii) moving the marker particles that show the fluid configuration.

The technique has been used for a variety of problems in the dynamics of incompressible fluids, including both confined and free surface flows. For the present example, several effects that the computing method can treat have been neglected: the drop and the pool are of the same fluid, viscosity and surface tension are negligible, and there are no buoyancy forces. Axial symmetry was assumed, with the use of the equations for cylindrical coordinates (*7*).

Figure 1 shows a sequence of fluid configurations for a calculation in which $R = 10.0$, $g = 0.1$, and $u_0 = 2.0$, so that $(gR)^{1/2}/u_0 = 0.5$. (These values establish the units of time used in the figure captions.) The pictures are exactly as obtained from the computer and processed through the Stromberg-Carlson SC-4020 microfilm recorder. At the initial time, the drop has just arrived at the surface of the pool. By the next frame, at a time (t) of 5.0, the pattern has already been established that leads to the late time distortions. Up to the time when $t = 20$, the crater continues to enlarge, and the layer of drop fluid grows thinner.

The first stage of collapse is shown at $t = 25$. Drop material slides down the sides and accumulates in a ring that bulges laterally into a pronounced concentration. (The lateral splash has hit the sides of the cylindrical container and is jetting upward.) Shortly thereafter, at $t = 30$, the collapse is at its most violent stage. Pressures rise at the axis, and the jet column is formed.

An enlargement of the configuration is shown in Fig. 2 for $t = 45$. The material originally in the drop is now in four principal regions: a deeply imbedded central slug, a lateral ring, a cone at the top of the jet column, and a droplet that is detaching at the top. The drop material in the cone tapers off laterally as a thin surface layer lying on top of the pool fluid.

Once the sequence of events is initiated, the processes contributing to the changes of configuration are evident from the figures. The most interesting part, therefore, is the earliest stage of the collision, prior to $t = 5$. To see what was happening, we examined the computer results in detail, and concluded the following.

1) Just before collision, the only vorticity is that which lies along the free surface of the drop. Its magnitude at any point on this surface is proportional to the sine of the angle from vertical.

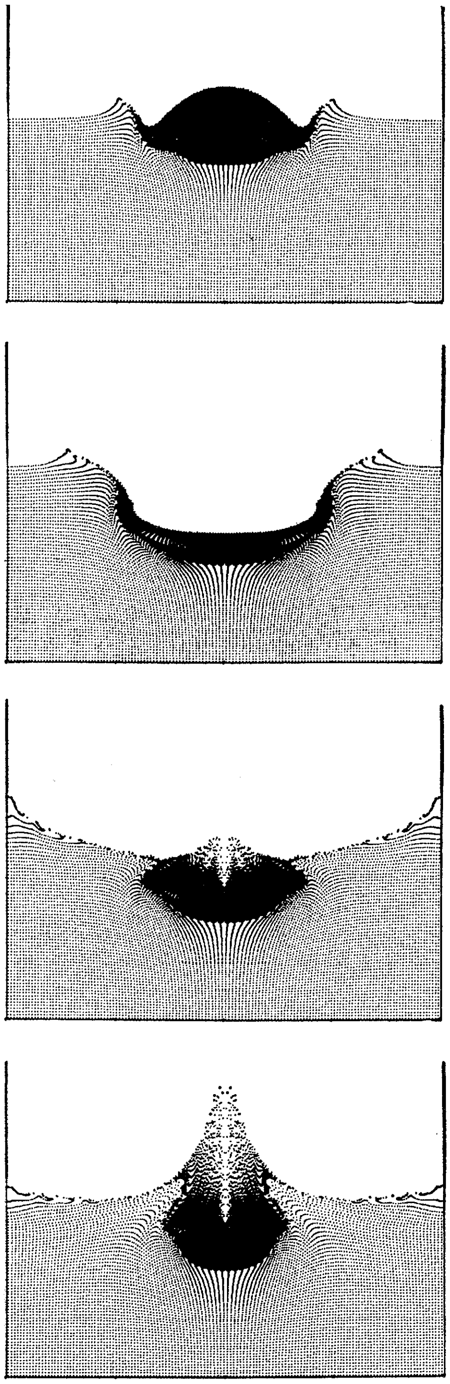

Fig. 3. Cross section of splashing drop with $u_0 = 1.0$. Frames are at $t = 10$, 20, 35, and 45.

2) During the earliest part of the collision, the surface is depressed, and the drop is deformed; both deformations producing an expanding flow.

3) The vortex layer is trapped between the drop and pool fluids.

4) As the angle of encounter increases, the gross-expansion flow is joined by a progressively more important skin jetting. Because of the vorticity, the jetted material comes mainly from the pool.

5) As a result, there is a disk-shaped vortex layer deposited in the fluid; its strength increases strongly with radius.

6) This vortex disk, closely resembling a smoke ring, projects fluid downward through its center, relative to the adjacent fluid, producing the configuration shown at $t = 5.0$ (Fig. 1).

When a drop collides with a rigid slick wall (or equivalently with another drop of equal size), then the lateral sheet jet becomes immediately noticeable (*4, 5*). The calculations for a drop hitting a flat pool surface, however, indicate that this jetting effect is significantly delayed.

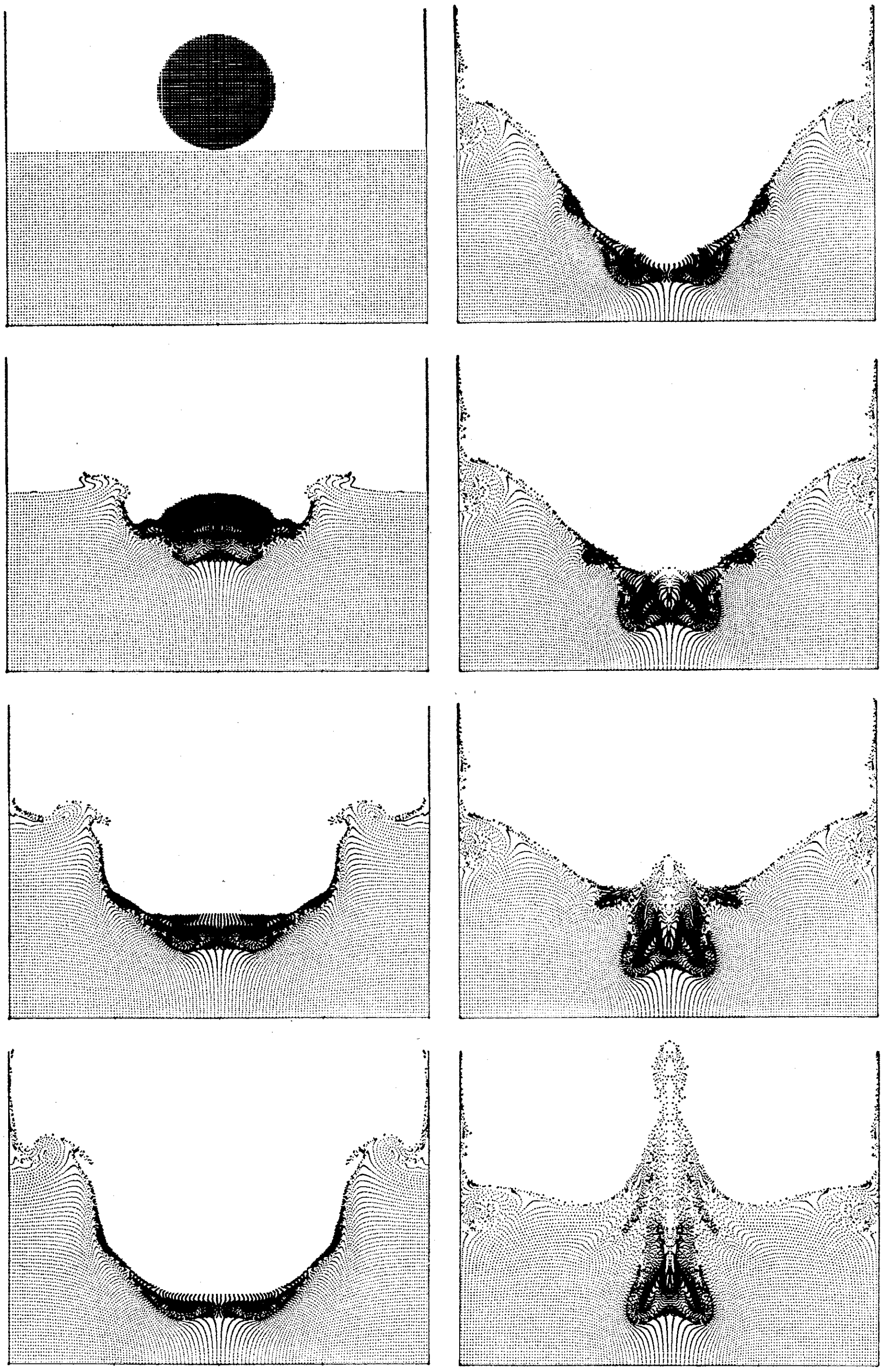

Fig. 4. Cross section of splashing drop with $u_0 = 4.0$. Frames (read left, down; right, down) are at $t = 0$, 5, 10, 15, 25, 28, 30, and 35.

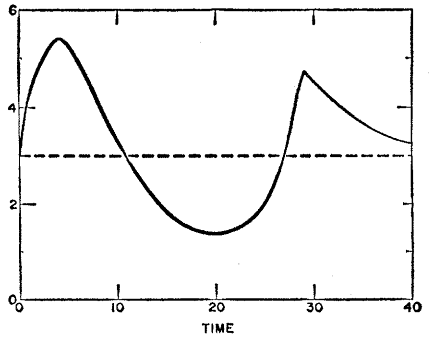

Fig. 5. Pressure history at the bottom of the pool for the calculation shown in Fig. 4.

The range of values for which the computer results exhibit the unusual drop deformation is $0.1 \lesssim (gR)^{1/2}/u_0 \lesssim 0.7$. At the lower value, the relatively violent crater collapse destroys the structure in its early stages; at the upper value, the lateral sag from the gravitational force obscures the effect.

Figure 3 shows the splash of a slower drop. The initial conditions are the same as for Fig. 1, except that $u_0 = 1.0$, so that $(gR)^{1/2}/u_0 = 1.0$. The contrast in sequence of configurations is apparent.

A fast drop, with $u_0 = 4.0$ and $(gR)^{1/2}/u_0 = 0.25$, is shown in Fig. 4. Several features distinguish this from the results of the slower drop. Even from the earliest times, the drop-pool interface near the axis is here concave downward. At $t = 28$, the collapse takes place below the ring bulge, while in Fig. 1 ($t = 30$) the collapse occurs above the ring bulge. As a result, the ultimate ring bulge is less prominent in the faster drop problem. In the last frame of Fig. 4 ($t = 35$), the detaching droplet is particularly well resolved by the calculation and shows the occurrence of detachment even in the absence of surface tension. The pressure as a function of time at the bottom of the pool, directly below the impact point, is plotted (Fig. 5) for the calculation in Fig. 4. The initial hydrostatic pressure is 3.0. Especially significant is the rapid rise in pressure at the time of crater collapse, which accelerates the fluid into the central jet column. Even though the dynamics appear violent in this example with $(gR)^{1/2}/u_0 = 0.25$, the drop had fallen a distance of only eight radii before collision. More rapid splashes exhibit a fascinating structure of their own, but have lost the intriguing ring bulge that occurs in this low-speed range.

FRANCIS H. HARLOW
JOHN P. SHANNON

University of California,
Los Alamos Scientific Laboratory,
Los Alamos, New Mexico 87544

References and Notes

1. P. V. Hobbs and A. J. Kezweeny, *Science* **155**, 1112 (1967).
2. B. K. Sahay, *Indian J. Phys.* **18**, 306 (1944).
3. H. E. Edgerton and J. R. Killian, Jr., *Flash* (Branford, Boston, 1954).
4. A. M. Worthington, *A Study of Splashes* (Macmillan, New York, 1963).
5. F. H. Harlow and J. P. Shannon, *J. Appl. Phys.*, in press.
6. F. H. Harlow, J. P. Shannon, J. E. Welch, *Science* **149**, 1092 (1965); F. H. Harlow and J. E. Welch, *Phys. Fluids* **8**, 2182 (1965); *ibid.* **9**, 842 (1966); B. J. Daly, *ibid.* **10**, 297 (1967).
7. J. E. Welch, F. H. Harlow, J. P. Shannon, B. J. Daly, *The MAC Method* (Los Alamos Scientific Laboratory, Los Alamos, New Mexico, 1966), Publication No. LA-3425.
8. Work sponsored by the Atomic Energy Commission.

12 June 1967

Chromatographic Silica Gel: Surface Area Determined by Adsorption

Abstract. *The surface area of silicic acid, a form of silica gel, has been determined by adsorption of methanol from a benzene solvent. The method is straightforward, uses inexpensive apparatus, and should be applicable to other particulate adsorbents.*

Surface areas of particulate solids are usually determined by the BET procedure (*1*), which involves gas adsorption at cryogenic temperatures; the apparatus is delicate and expensive, and requires a skilled operator for reliably accurate results. In an effort to simplify determinations of area and to avoid the complicated BET apparatus, Nelsen and Eggertsen (*2*) devised a continuous-flow method that is based on changes in thermal conductivity exhibited by a gaseous adsorbate stream as it is passed over the solid at cryogenic temperatures; their approach provided good agreement with standard BET determinations. Later, Roth and Elwood (*3*) adapted a gas chromatograph to this continuous-flow method. A commercial instrument that measures surface area and pore volume, and whose design is based on the Nelsen-Eggertsen concept, is on the market.

After Frankel *et al.* (*4*) developed a liquid-chromatographic system based on methanol-benzene–silicic acid (SiO_2), we evaluated the parameters essential to the system (*5*). In an attempt to determine chromatographic mechanisms that influence separations of lipid materials on silicic acid, we turned to evaluation of solvent systems other than methanol-benzene (*6*). From a third investigation and the two immediately preceding we established the validity of the general chromatographic formula that Frankel *et al.* (*4*) had found empirically to be useful for lipid materials. Indeed their empirical formula is based on a solvent-adsorbent combination wherein methanol is adsorbed on the silica to a level of concentration representative of monolayer coverage. Under these conditions, lipid materials during fractionation received efficient competition from methanol for active sites on the silica, and therefore eluted as sharp peaks exhibiting quantitatively useful resolution within practical time limits.

Table 1. Adsorbate-adsorbent relations that allow calculations of surface area from alcohol adsorption data. Areas per molecule based on the assumption of spherical shape. N_o, Avogadro number.

Solute	Conc. in supernatant (vol. % in benzene)	Alcohol Adsorbed On SiO_2 (Moles × 10^{-3})/g	Gram/gram	Molecules (N_o) (moles × 10^{20})	Area per: Molecule (Å^2)	Gram of SiO_2 (m^2)
Methanol	0.90	4.50	0.145	27.1	19.9	540
Ethanol	1.00	3.10	0.144	18.6	25.5	474
1-Propanol	0.95	2.43	0.145	14.5	30.2	438
2-Propanol	0.90	2.41	0.146	14.6	30.8	450
1-Butanol	0.80	1.98	0.147	11.9	34.4	409

Figure 1 shows typically Langmuir-type adsorption isotherms for five aliphatic alcohols adsorbed on 50 g of silicic acid from 100 ml of benzene. Each alcohol was added to the adsorbent at concentrations of 4, 8, 16, 32, and 50 percent by weight. Relative concentrations of adsorbed and unadsorbed methanol were determined from an ordinary calibration plot of solution refractive index versus known alcohol concentration (*6*). Solution compositions were converted to mole percentages for isotherm plots. Extrapolation of the linear portions of these isotherms enabled determination of each isotherm "knee"—a point at which the alcohol adsorbate is conventionally assumed to exist on the silica surface as a monolayer (*7*). Table 1 lists, among other data, solute-solvent relations pertinent to the isotherms.

It seemed likely that methanol adsorption on silica might be a means of determining surface area. If one assumes that alcohols are spherical molecules, and on the basis of knowledge of the molecular weight and density of each, one can calculate the cross-sectional area of one molecule.

The last five columns of Table 1 contain necessary information for relating solute cross section with the true area covered by the alcohol adsorbed at monolayer concentration; Fig. 2 graphically depicts this relation. Deviation of the plot from infinite slope (vertical) is a measure of the error introduced by assumption that the alcohols are spherical molecules. Obviously they are not; if they were simply spheres of increasing size, each would be sterically adsorbed to an extent proportional to its radius. For example, butanol has twice the carbon content of ethanol and thus about twice the assumed circular cross section; SiO_2 should therefore adsorb only half as much butanol as ethanol. The data point for butanol would lie directly below that for ethanol, since a circle representative of one butanol molecule could cover twice the area of one for ethanol. Since butanol does not lie below ethanol, an assumption of sphericity becomes in greater error as the

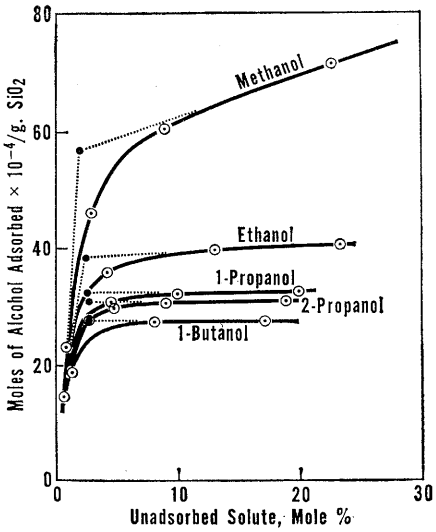

Fig. 1. Aliphatic-alcohol adsorption isotherms on silicic acid, from benzene.